


Silicon Photonic Wires for Broadband Polarization Entanglement at Telecommunication Wavelengths

Shivani Sharma¹, Vivek Venkataraman, and Joyee Ghosh^{1*}

Department of Physics, Indian Institute of Technology Delhi, New Delhi 110016, India

 (Received 27 November 2021; revised 30 June 2022; accepted 6 September 2022; published 18 October 2022)

We present designs for silicon-on-insulator nanowaveguide sources capable of generating polarization-entangled photon pairs with high concurrence (approximately 0.98) across the S, C, and L bands (approximately 1475–1625 nm) in the telecommunications spectrum via degenerate-pump spontaneous four-wave mixing. Silica-clad waveguides with Si film thickness 280 nm, width in the range 700–800 nm, and length up to 1 cm are shown to be optimum, generating near-perfect entangled pairs over a bandwidth >100 nm around 1550 nm. Further, the use of relatively narrow pump bandwidths (<10 GHz) can still yield a concurrence > 0.95 in waveguides up to 7 mm long despite the presence of large polarization-mode dispersion in these high-index-contrast structures. Such broadband integrated sources can be employed in multichannel wavelength-division multiplexed entanglement-based quantum key distribution protocols over standard optical-fiber networks.

DOI: [10.1103/PhysRevApplied.18.044043](https://doi.org/10.1103/PhysRevApplied.18.044043)

I. INTRODUCTION

Photonic qubits stand out as entanglement sources that are useful for quantum communication [1,2], computation [3], teleportation [4,5], metrology [6], simulation [7], entanglement swapping [8], and key distribution protocols [9,10], due to their robustness to decoherence and applicability in long-distance quantum information networks [11,12]. Polarization-encoded qubits in particular provide an ideal two-level system, offering relatively greater ease of generation, manipulation, and measurement of entangled quantum states in standard bulk and integrated optical setups [13]. This advantage propels the need for polarization-entangled photon-pair sources in the telecommunications regime that can employ the existing well-developed network of optical fibers around the wavelength of 1.55 μm .

Advances in integrated quantum photonics are particularly important for hastening the course of miniaturization and for improvement in the stability and scalability of quantum information technology. Concerted efforts have been made toward designing all-optical quantum networks with functionalities such as filters and single-photon detectors on the same chip [14–16], where photon sources remain the primary building blocks. Entangled photon-pair sources based on spontaneous parametric down-conversion (SPDC) [17–19] in $\chi^{(2)}$ waveguides are not amenable to large-scale integration and additionally face a

drawback of timing jitter [20], requiring intricate engineering such as periodic poling and/or material birefringence to attain phase matching. On the contrary, in spontaneous four-wave mixing (SFWM) based $\chi^{(3)}$ devices [21–26], the phase-matching condition can be flexibly achieved via dispersion engineering. Here, dispersion-shifted fiber (DSF) has been employed for entanglement generation [22,27]; however, the purity and efficiency have largely been limited by the noise photons arising due to spontaneous Raman scattering (SpRS) [28]. Researchers have circumvented the problem by using liquid nitrogen as a coolant for the fibers, which, however, complicates the experimental setup [21,29]. Sources based on a silicon-on-insulator (SOI) platform are also a promising candidate for integrated quantum photonics due to the mature and cost-effective fabrication technology. Moreover, crystalline silicon has a well-defined narrow (approximately 100-GHz) SpRS spectrum, which is 15 THz away from the pump [30], whereby the noise photons can be easily eliminated either via filtering or by ensuring appropriate pump-signal detuning. Additionally, the large effective nonlinearity of approximately 10^5 times larger as compared to silica fibers [31] and the high refractive-index contrast ($\Delta n \sim 2$) in SOI waveguide structures aids in efficient nonlinear interaction at low powers along with dispersion engineering via tailoring the waveguide dimensional parameters for different applications.

Since the demonstration of correlated photon pairs from Si nanowaveguides [32], there have been a number of reports concerning time-bin-entangled photon pairs [24,33]; however, not much work has been done toward

*joyee@physics.iitd.ac.in

polarization-encoded qubits. The predominant reason is that the high asymmetry in conventional SOI waveguides [typically referred to as silicon wire waveguides (SWWs)], with a standard Si film thickness of approximately 220 nm, does not allow the fundamental quasitransverse magnetic (TM_{00}) mode to be well guided [20]. Polarization entanglement has been demonstrated in a SOI waveguide using a Sagnac fiber loop and a polarizing beam splitter, which adds complexity to the experimental setup precluding scalability [34]. Though improvements for eliminating off-chip optical elements such as two-dimensional (2D) coupler combined nanowaveguides for a direct path to polarization conversion [35] and the Si-based polarization rotator [14] have been experimentally demonstrated, there have been no instances of direct generation of polarization entanglement utilizing both fundamental quasi-TE and quasi-TM modes except for Ref. [36], which employs the technique of optimizing the polarization angle of the pump. However, the separation of entangled channels from the pump in this work is just approximately 3 nm, limited by the high group-velocity dispersion yielded by the TM mode at $1.55 \mu\text{m}$ [36], in contrast to the recent 60-nm SFWM bandwidth demonstrated in deeply etched (Al,Ga)As waveguides [26]. Our work takes this forward to theoretically explore dispersion engineering in SOI waveguides in order to achieve broadband polarization entanglement, in addition to optimization of the polarization angle of the pump to achieve a maximally entangled state. We theoretically demonstrate the generation of broadband polarization entanglement in SOI waveguides with a very high concurrence utilizing both H and V polarizations without requiring off- or on-chip polarization rotators or adjustment of the pump polarization.

In this paper, we numerically simulate silica-clad SOI waveguides with a larger ($> 220\text{-nm}$) Si film thickness (or waveguide height) to investigate the optimum dimensions for achieving a broad SFWM bandwidth for both all-TE and all-TM SFWM processes. Further, the concurrence is computed and plotted as a function of the pump-signal (idler) detuning for the optimized waveguides. The optimization of the polarization angle of the pump to further compensate the unequal nonlinear strengths of the two scalar SFWM processes to achieve maximal entanglement of the two-photon state is also discussed. Finally, the last section discusses the degradation of entanglement due to polarization-mode dispersion (PMD).

The proposed waveguide designs could be useful as building blocks in quantum communication networks that rely on entanglement-based key distribution protocols. A SFWM bandwidth of approximately 150 nm for both of the polarizations permits a large number of polarization-entangled channels (on either side of the pump at 1550 nm) covering nearly the entire S, C, and L bands in the telecommunications spectrum, thereby efficiently utilizing the existing optical-fiber network. The entanglement

multiplexing (> 50 channels) [26] offered by such integrated devices can help in increasing the data rates and/or the number of simultaneous users in quantum communication.

II. THEORY

SFWM is a third-order nonlinear optical phenomenon in which two photons at frequencies ω_s and ω_i (called the signal and idler, respectively) are created when two pump photons at frequency ω_p annihilate such that $2\omega_p = \omega_s + \omega_i$.

When a pump with polarization angle θ (with the H direction corresponding to the polarization of the TE mode) is incident on a Si nanowaveguide [see Fig. 1(a)], there are in general, two types of SFWM interactions possible: scalar and vector. The scalar process is where H- (V-) polarized pump photons generate signal and idler photons in the same H- (V-) polarization state; whereas the vector process involves the generation of signal and idler photons with orthogonal polarization. In this paper, we designate all processes as “ $mnrq$,” where m , n , q , and r denote the polarization of the two pump, signal, and idler photons, respectively ($m, n, q, r \in \{H, V\}$). Therefore, HHHH and VVVV refer to the scalar processes and HVHV, HVVH, VHVH, and VHHV are the vector processes. The symmetry in the third-order susceptibility tensor of crystalline silicon [37] allows eight SFWM interactions overall. The other two possible SFWM processes (HHVV and VVHH) are not phase matched due to large PMD in SOI waveguides [38] and thereby can be omitted from the discussion.

The most general expression for the output state can be worked out using the backward Heisenberg approach under the no-pump depletion condition (some intermediate steps are given in the Supplemental Material [39]) and can be written as [40,41]

$$|\psi_{\text{out}}\rangle = \sum_{mnrq} \alpha_m \alpha_n \int \int d\omega_s d\omega_i F(\omega_s, \omega_i) \times \phi_{mnrq}(\omega_s, \omega_i) |q, \omega_s; r, \omega_i\rangle. \quad (1)$$

The summation is over m , n , q , and r to take into account the contribution from all possible configurations of SFWM processes. $|\alpha_j|^2$ gives the number of photons (proportional to the pump power) present in the “ j ” pump polarization. $F(\omega_s, \omega_i)$ is the spectral transmission function for the signal and idler filters, used for collecting the photons at the output. $\phi_{mnrq}(\omega_s, \omega_i)$ can be termed the biphoton wave function (BWF) corresponding to the “ $mnrq$ ” process, which contains the information about the pump spectra as well as the phase-matching function and thereby characterizes the correlations/entanglement present between the

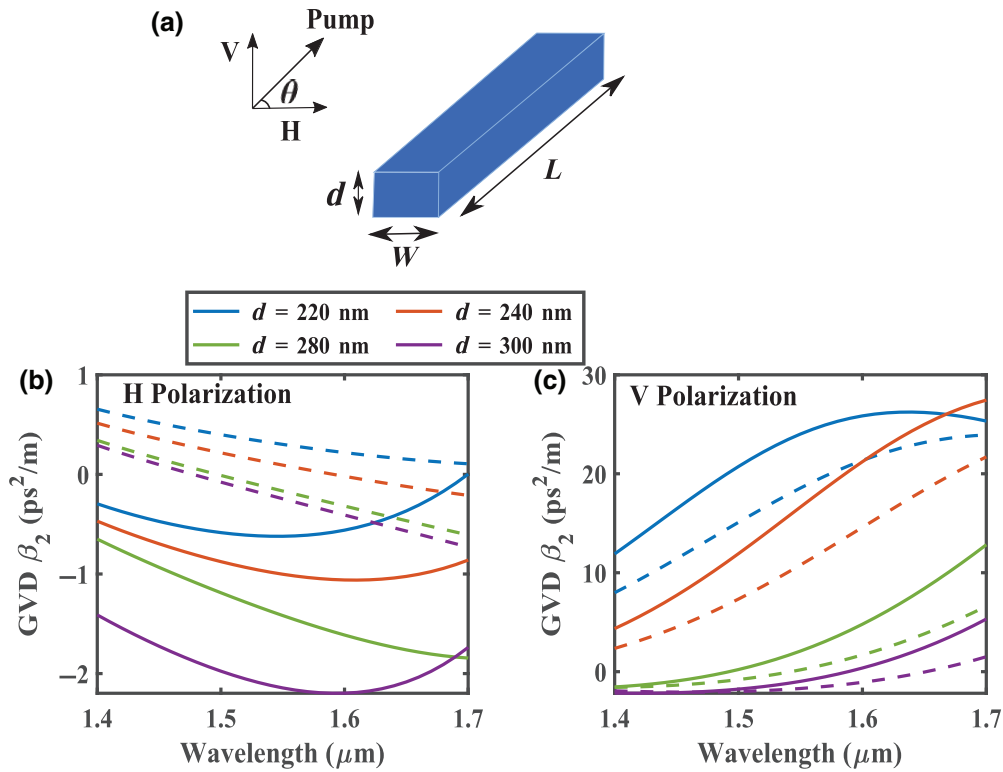


FIG. 1. (a) A schematic of the core of the Si nanowaveguide with height (silicon-film thickness) d , width W , and length L . (b),(c) The group-velocity dispersion β_2 (GVD) as a function of the wavelength for waveguide widths of 500 nm (solid lines) and 700 nm (dashed lines) for different heights d for (b) the fundamental TE mode (H polarization) and (c) the fundamental TM mode (V polarization). θ , Polarization angle.

paired photons. The BWF can be expressed as [26]

$$\begin{aligned}
 \phi_{mnqr}(\omega_s, \omega_i) &= K \int d\omega \operatorname{sinc} \left[\frac{\Delta\beta_{mnqr}L}{2} \right] \\
 &\times \exp \left[i \frac{\Delta\beta_{mnqr}L}{2} \right] \phi_m(\omega) \phi_n(\omega_s + \omega_i - \omega) \\
 &\times \frac{1}{\sqrt{v_{gm}(\omega)v_{gn}(\omega_s + \omega_i - \omega)v_{gq}(\omega_s)v_{gr}(\omega_i)}} \\
 &\times \sqrt{\omega(\omega_s + \omega_i - \omega)\omega_s\omega_i}, \quad (2)
 \end{aligned}$$

where $v_{gm(n,q,r)}(\omega)$ is the group velocity of the field with polarization $m(n, q, r)$ at frequency ω and $\phi_j(\omega)$ is the pump-envelope spectral profile corresponding to the “ j ” pump polarization. L is the waveguide length and $\Delta\beta$ is the linear phase mismatch corresponding to the “ $mnqr$ ” process, which is given by

$$\Delta\beta_{mnqr} = \beta_{mp} + \beta_{np} - \beta_{qs} - \beta_{ri}, \quad (3)$$

where $\beta_{mp(np,qs,ri)}$ is the propagation constant for polarization $m(n, q, r)$ at frequency $\omega_{p(p,s,i)}$. The phase mismatch depends to a considerable extent on the group-velocity

dispersion (GVD) parameter β_2 (see the Supplemental Material [39]), which in turn depends on the material and waveguide geometry. Note that the nonlinear part of the phase mismatch can be neglected for pump powers less than 100 mW (for waveguide lengths up to a few centimeters), the required regime of operation for ensuring that multiphoton pair-generation events can be neglected [42]. Also, the conservation of energy is already embedded in the expression.

In Eq. (2), K is a proportionality constant that incorporates the nonlinear strength, which depends on the susceptibility component $\chi_{mnqr}^{(3)}$ and the mode overlap factor f_{mnqr} between the fields with polarizations m, n, q , and r involved in the SFWM “ $mnqr$ ” process. The inverse of the overlap factor, f_{mnqr} [43], has the units of area and hence can be treated as being equivalent to the effective modal area A_{mnqr} .

The resultant output state is, in general, a superposition of |HH>, |VV>, |HV>, and |VH>. It is evident that each of these states results from summing over both pump polarizations and integrating over all frequencies. Silicon is a cubic crystal that possesses $m3m$ point-symmetry and therefore $\chi^{(3)}$ has only two independent elements, $\chi_{1111}^{(3)}$ and $\chi_{1122}^{(3)}$ ($\chi_{1111}^{(3)} = 2.36\chi_{1122}^{(3)}$) [44]. Therefore, the vector SFWM processes HVVV and VHHH are not allowed.

Further, entanglement can be quantified by a parameter called the concurrence, which for a two-qubit pure state $c_{HH} |HH\rangle + c_{VV} |VV\rangle + c_{HV} |HV\rangle + c_{VH} |VH\rangle$ can be evaluated as follows [45]:

$$C = 2|c_{HH}c_{VV} - c_{HV}c_{VH}|, \quad (4)$$

where c_{qr} are the four coefficients that can be computed using Eq. (1). Here, we focus on the generation of the symmetric Bell state, requiring the coefficients c_{HV} and c_{VH} to vanish, so that the output state is

$$|\psi_{\text{out}}\rangle = c_{HH} |HH\rangle + c_{VV} |VV\rangle. \quad (5)$$

The maximum entanglement or unit concurrence for the above Bell state is achieved when $|c_{HH}|$ and $|c_{VV}|$ are equal ($1/\sqrt{2}$ for a normalized state). This condition demands the fundamental quasi-TE and quasi-TM modes of a waveguide (which here correspond to H and V polarizations, respectively) to be identical with respect to certain properties such as field confinement and dispersion, so that all-TE (HHHH) and all-TM (VVVV) SFWMs yield nearly equal photon-generation rates. The most naive solution seems to be to employ waveguides with square cores; however, in such cases, the vector SFWM processes also contribute considerably (i.e., c_{VH} and c_{HV} are not negligible), leading to factorizability in the generated state.

The conventional Si wire waveguides with 220-nm film thickness do not guide the TM mode well; therefore, it is necessary to optimize the waveguide height (to minimize the waveguide asymmetry) such that rate of generation of $|HH\rangle$ and $|VV\rangle$ can be nearly equalized while the vector processes generating $|HV\rangle$ and $|VH\rangle$ are also suppressed. Further, for broadband polarization entanglement, HHHH and VVVV processes should also exhibit nearly equal and broad operating bandwidths that can be achieved via waveguide-width optimization for a chosen waveguide height [42] (Note that the SFWM bandwidth values reported in this work are calculated considering $\Delta\beta < |\pi/L|$ as the tolerance limits of the phase mismatch and the pump wavelength is also fixed at 1550 nm.) Therefore, it is imperative to maximize the concurrence by optimizing the phase mismatch (via dispersion engineering), the relative pump powers in each polarization (via the input polarization angle of the pump), the pump bandwidth (by including the effect of PMD), and the waveguide length.

III. RESULTS

A. Dispersion engineering

1. Optimization of the waveguide height

It is already emphasized above that the standard silicon thickness [or waveguide height d ; see the schematic in Fig. 1(a)] of 220 nm in conventional Si waveguides does

TABLE I. The SFWM bandwidth around $1.55 \mu\text{m}$ yielded by different waveguide widths for the two scalar processes for a waveguide height of 280 nm and a waveguide length of 1 cm.

Width (nm)	Bandwidth yielded in HHHH process (nm)	Bandwidth yielded in VVVV process (nm)
700	110	95
750	350	130
770	150	150
800	100	160

not allow the fundamental quasi-TM mode to be well confined. For example, in a silica-clad SOI waveguide with cross section $220 \times 500 \text{ nm}^2$, the effective refractive index is 2.4484 for TE_{00} and 1.7728 for TM_{00} at a wavelength of $1.55 \mu\text{m}$. Moreover, the achievable bandwidths for all-TE (HHHH) and all-TM (VVVV) SFWM processes are also different due to the different group-velocity dispersion ($-0.62 \text{ ps}^2/\text{m}$ for TE_{00} and $24.02 \text{ ps}^2/\text{m}$ for TM_{00} at $1.55 \mu\text{m}$ (see the Supplemental Material [39]). Both of these effects degrade the concurrence and therefore act as limitations to the generation of broadband polarization entanglement.

The fundamental TE and TM modes are extensively simulated for a wide range of heights (220–300 nm) and widths (400–800 nm) of silica-clad SOI waveguides to investigate the variation of group-velocity dispersion (GVD, β_2) which predominantly determines the phase mismatch (see the Supplemental Material [39]). The GVD is shown in Figs. 1(b) and 1(c) as a function of the wavelength for widths of 500 nm and 700 nm for both H and V polarizations. It can be observed that the fundamental TE mode yields near-zero GVD (-2 to $1 \text{ ps}^2/\text{m}$) at $1.55 \mu\text{m}$ for all heights varying from 220 to 300 nm; however, β_2 at $1.55 \mu\text{m}$ for the fundamental TM mode approaches zero only for a height in the range 280–300 nm. Therefore, $d \sim 280\text{--}300 \text{ nm}$ can be chosen to achieve a reasonable phase-matching bandwidth for V polarization as well. However, for entanglement, all-TE (HHHH) and all-TM (VVVV) both should yield a nearly equal and broad bandwidth for a particular waveguide cross section.

2. Width optimization

Next, the GVD parameter β_2 at the pump wavelength of $1.55 \mu\text{m}$ is studied as a function of the waveguide width [see Fig. 2(a)] for $d = 280 \text{ nm}$ and 300 nm . It is evident that the H and V polarizations both have near-zero and approximately equal GVD values for widths around approximately 770 nm for $d = 280 \text{ nm}$ and approximately 530 nm for $d = 300 \text{ nm}$ (the intersections are encircled in blue and red, respectively). However, the bandwidth common to both HHHH and VVVV processes for $d = 300 \text{ nm}$ is lower than $d = 280 \text{ nm}$ due to the relatively higher GVD. This can be understood more clearly by looking

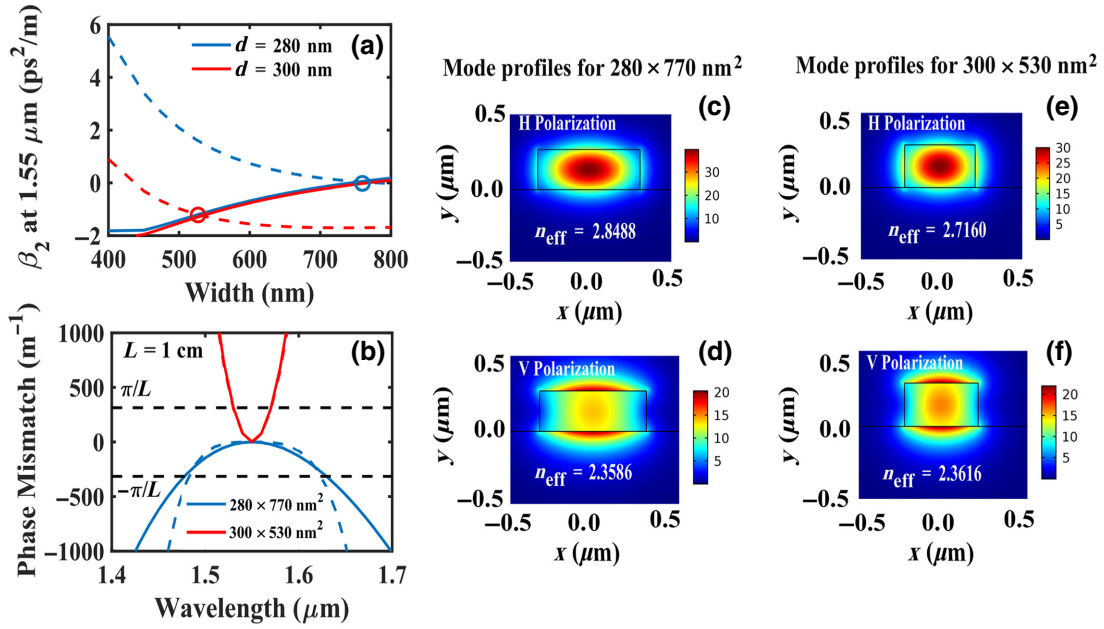


FIG. 2. (a) The group-velocity dispersion (GVD) exhibited by the fundamental TE (H, solid lines) and TM mode (V, dashed lines) at $1.55 \mu\text{m}$ as a function of the waveguide width W for $d = 280 \text{ nm}$ and $d = 300 \text{ nm}$. (b) The phase mismatch as a function of the wavelength for HHHH (solid lines) and VVVV (dashed lines) processes for waveguide cross sections $280 \times 770 \text{ nm}^2$ (blue circle) and $300 \times 530 \text{ nm}^2$ (red circle), waveguide length $L = 1 \text{ cm}$, and a pump wavelength of $1.55 \mu\text{m}$. (c)–(f) Mode profiles for the fundamental TE mode (H polarization) and the fundamental TM mode (V polarization) for (c),(d) $280 \times 770 \text{ nm}^2$ and (e),(f) $300 \times 530 \text{ nm}^2$.

at the phase-mismatch curves for the HHHH and VVVV processes [see Fig. 2(b)] for waveguide cross sections $280 \times 770 \text{ nm}^2$ and $300 \times 530 \text{ nm}^2$, yielding common bandwidths of approximately 150 nm and approximately 40 nm, respectively. The fundamental mode profiles at $1.55 \mu\text{m}$ for both the polarizations are shown for the optimum waveguide dimensions, i.e., $280 \times 770 \text{ nm}^2$ and

$300 \times 530 \text{ nm}^2$, in Figs. 2(c), 2(d), 2(e), and 2(f). Clearly, the difference in the effective indices and hence the difference in the degree of confinement between the two polarizations is comparatively lower than that for a waveguide with the standard SOI thickness, e.g., $220 \times 500 \text{ nm}^2$ (see the Supplemental Material [39]). Further, the bandwidths yielded by widths in the range 700–800 nm for $d = 280 \text{ nm}$ are listed in Table I, which shows that a bandwidth $> 100 \text{ nm}$ can be obtained for polarization entanglement for this width range. $W = 770 \text{ nm}$ yields the maximum common bandwidth of 150 nm around 1550 nm, covering nearly the entire S, C, and L bands in the telecommunications spectrum.

3. Suppression of vector processes

Another essential condition for a maximally entangled state is to ensure suppression of the vector processes taking place, viz., HHVV, VVHH, HVHV, VHVH, HVVH, and VHHV. HHVV and VVHH are not phase matched, while HVHV and VHVH are phase matched only for a very small range of frequency around the pump. This is elaborated in Fig. 3, which shows the normalized BWF for the four states $|\phi_{HH}\rangle$, $|\phi_{VV}\rangle$, $|\phi_{HV}\rangle$, and $|\phi_{VH}\rangle$ for a waveguide with cross section $280 \times 700 \text{ nm}^2$ and a length L of 1 cm. The pump spectral profile is taken to be Gaussian, with a bandwidth of 500 GHz around 1550 nm.

The BWFs are calculated using Eq. (2) by integrating over all the pump frequencies and also taking into

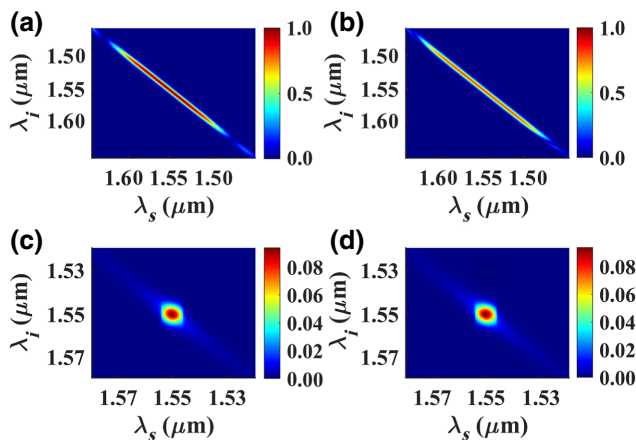


FIG. 3. The normalized BWF ($|\phi_{qr}\rangle$) for the four states (a) $|\phi_{HH}\rangle$, (b) $|\phi_{VV}\rangle$, (c) $|\phi_{HV}\rangle$, and (d) $|\phi_{VH}\rangle$ for waveguide cross section $280 \times 700 \text{ nm}^2$, waveguide length $L = 1 \text{ cm}$, a pump wavelength of 1550 nm , and a pump bandwidth taken as 500 GHz.

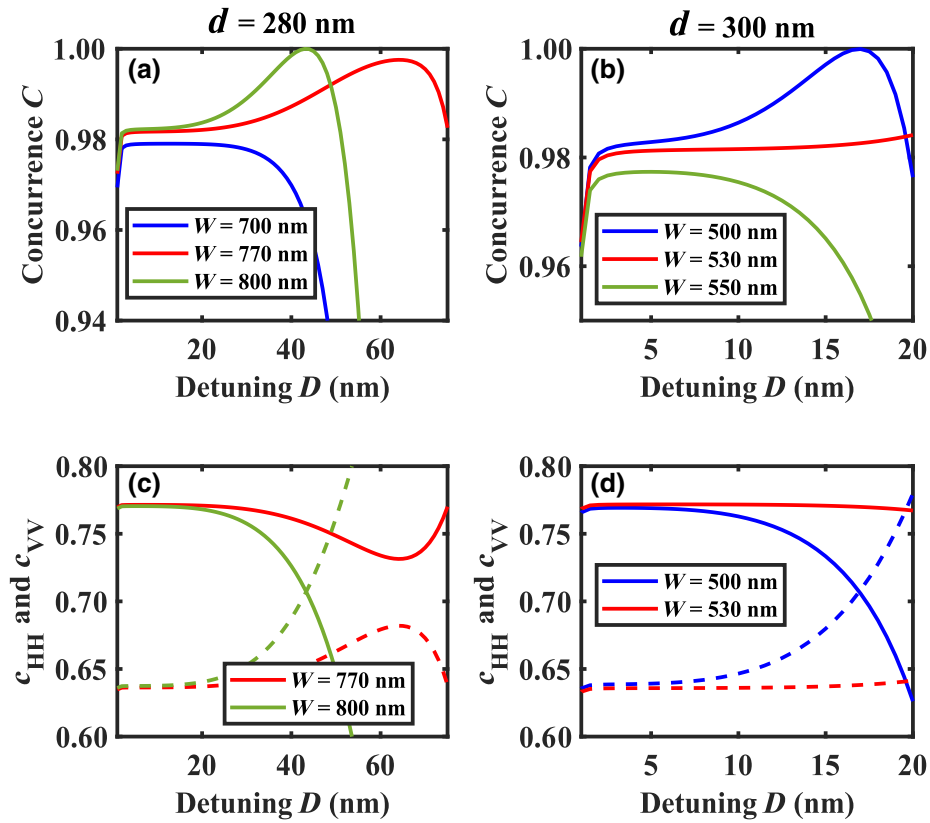


FIG. 4. (a),(b) The concurrence C as a function of the detuning D for different waveguide widths and heights: (a) $d = 280$ nm and (b) $d = 300$ nm. (c),(d) The coefficients c_{HH} (solid lines) and c_{VV} (dashed lines) as a function of the detuning D for (c) $d = 280$ nm and (d) $d = 300$ nm. All the calculations assume a pump wavelength of 1550 nm, a waveguide length of 1 cm, and a pump and filter bandwidth of 100 GHz each.

account both pump polarizations. Figures 3(a) and 3(b) show the BWF for the dominant states $|HH\rangle$ and $|VV\rangle$, which clearly reveals that the scalar processes are phase matched and the generated photons are correlated for a large range of signal or idler wavelengths (approximately 1.5–1.6 μm). The other two BWFs resulting from vector processes [Figs. 3(c) and 3(d)] are phase matched for a very small range of wavelengths (approximately 2 nm) around the pump, which implies that these can be easily suppressed by just ensuring that the pump-signal or idler detuning is greater than 1 nm. Moreover, the vector BWFs have much lower intensity. Note that BWFs for other optimum waveguide dimensions (i.e., width 700–800 nm for $d = 280$ nm) will also be qualitatively similar except for a scaling factor depending on the relative phase-matching bandwidths.

B. Concurrence

The degree of polarization entanglement achievable from the proposed waveguide sources can be quantified by computing the concurrence, which is given by Eq. (4). The four coefficients c_{HH}, c_{VV}, c_{HV} , and c_{VH} can be evaluated

by inserting the BWFs in Eq. (1), taking the spectral profile for the input pump and optical filters at the output as Gaussian functions:

$$\phi_p(\omega_s, \omega_i) = \exp\left[-\frac{(\omega_s + \omega_i - 2\omega_{po})^2}{2\sigma_p^2}\right], \quad (6)$$

$$F_{s(i)}(\omega_{s(i)}) = \exp\left[-\left(\frac{\omega_{s(i)} - \omega_{so(io)}}{\sigma_{s(i)}}\right)^2\right]. \quad (7)$$

Here, ω_{po} and σ_p refer to the central frequency and bandwidth of the pump pulses, respectively. $\omega_{so(io)}$ and $\sigma_{s,i}$ are the central frequency and bandwidth of the optical filter used in the signal (idler) arm, respectively. If D is the pump-signal or idler detuning, then central frequencies are given by

$$\omega_{io(so)} = \omega_p \pm D. \quad (8)$$

We now discuss the concurrence achievable in the optimum waveguide dimensions obtained via dispersion engineering in the previous sections, i.e., waveguides with

heights of 280 nm and 300 nm. Figures 4(a) and 4(b) show the concurrence plotted as a function of the detuning D for a few widths around the optimal 770 nm for $d = 280$ nm and 530 nm for $d = 300$ nm, respectively. A waveguide length of 1 cm, pump and output filter bandwidths (σ_p and $\sigma_{s,i}$) of 100 GHz each, and a pump wavelength of 1550 nm are considered for all these calculations. Note that all the curves start with a slightly lower concurrence due to the considerable contribution from the states $|HV\rangle$ and $|VH\rangle$ at such small detuning (approximately 1 nm), as discussed in the Sec. III A.

Figure 4(a) shows that a concurrence $\gtrsim 0.98$ is achievable up to wavelength detunings of 30 nm, 50 nm, and 75 nm through waveguides with widths of 700 nm, 770 nm, and 800 nm (for a fixed height of 280 nm), respectively. Note that while the concurrence is nearly constant for 700 nm, it increases and reaches approximately 1 for 770 nm and 800 nm. The exact intricate behavior of the concurrence with detuning is determined by the spectral dependence of the phase mismatch. For example, see Fig. 2(b), where the phase mismatch (blue lines for $W = 770$ nm) for VVVV is lower than for HHHH up to a certain detuning, which, to some extent, compensates for the different effective nonlinear strengths of the two processes. This explains the cases for 770 nm and 800 nm, which can also be understood better from Fig. 4(c), where the coefficients become equal at a detuning of approximately 45 nm and the concurrence becomes 1 for $W = 800$ nm.

Similarly, the concurrence is plotted for widths around 530 nm for a height of 300 nm in Fig. 4(b). It is observed that the concurrence $C \gtrsim 0.95$ for widths of 500 nm, 530 nm, and 550 nm for wavelength detuning $D \lesssim 20$ nm. $W = 500$ nm shows the unit concurrence at a detuning of 17 nm for a similar reason as mentioned above [see c_{HH} and c_{VV} intersecting in Fig. 4(d)].

It can be inferred from the above discussion that waveguides with a height of 280 nm can yield a nearly constant high concurrence ($C > 0.95$) for a large wavelength range > 100 nm (maximum 150 nm) for widths in the range 700–800 nm. On the other hand, for waveguides with $d = 300$ nm, the maximum wavelength range for achieving a high concurrence ($C > 0.95$) is limited to 40 nm for widths in the range 500–550 nm. Since the main objective of this paper is broadband polarization entanglement, in the rest of the paper we discuss the most optimal waveguide with dimensions 280×770 nm².

1. Optimizing the polarization angle of the pump

Up to now, the concurrence is evaluated taking equal pump powers in both (H and V) polarizations [$\theta = 45^\circ$ or $\alpha_H = \alpha_V$; see Eq. (1)]. However, it can be seen that the probability of generation of a particular state also depends on the effective pump power, in addition to the nonlinearity, which varies inversely with the effective modal

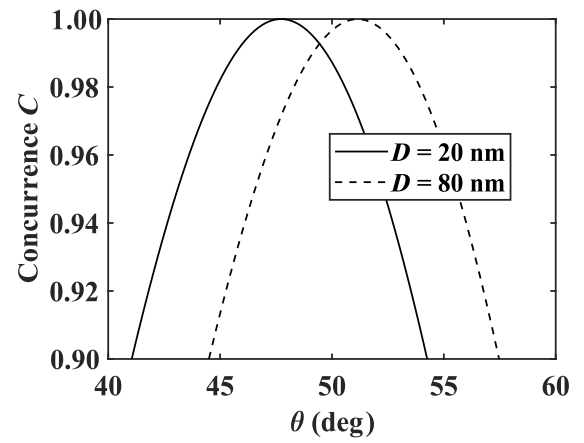


FIG. 5. The concurrence C as a function of the polarization angle of the pump θ for 280×770 nm² at different detunings of 20 nm and 80 nm.

area ($\gamma = \omega n_2 / c A_{\text{eff}}$, where n_2 is the nonlinear coefficient for silicon). Therefore, unequal pump powers can also be used to compensate for different degrees of field confinement in both the polarizations (i.e., injecting more power in the polarization with weaker confinement). It is thus useful to have *a priori* knowledge of the optimum input-pump polarization angle θ for a given waveguide structure. Figure 5 shows the variation of the concurrence with the change in pump angle θ for the optimum waveguide cross section 280×770 nm² at detunings of $D = 20$ nm (solid) and $D = 80$ nm (dashed). The concurrence can be enhanced from 0.98 to 1 by setting the pump polarization to approximately 47° at a detuning of 20 nm. The slight variation of the optimum angle with detuning can again be exactly understood through the spectral dependence of the phase mismatch. However, the variation is small and an angle can always be chosen to obtain a high concurrence (> 0.98) over the entire phase-matching bandwidth (for additional details, see the Supplemental Material [39]).

Experimentally, the rates can be equalized by preparing the pump at the required angle using standard optical components such as a half-wave plate and a polarization controller before coupling light into the waveguide [26,36]. Light is coupled in and out of the waveguide using either lensed fibers and inverse tapering (in-plane) or integrated grating couplers (out of plane) at both ends of the waveguide [46]. However, the typical lengths involved in the nanotaper [47] and grating coupler [48] are < 100 μm and therefore do not affect the synchronization of the H and V polarizations at the waveguide input.

2. Effect of PMD on concurrence: Optimization of waveguide length and pump bandwidth

Arising due to the waveguide asymmetry in our case, PMD implies that the H and V polarizations travel with different group-velocities, which leads to a temporal lag

(also called the differential group delay) between the states $|HH\rangle$ and $|VV\rangle$, given by [for the signal (τ_s) and the idler (τ_i)]

$$\tau_{s(i)} = L \left(\frac{1}{v_g(H, \omega_{s(i)})} - \frac{1}{v_g(V, \omega_{s(i)})} \right). \quad (9)$$

Consequently, the temporal distinguishability between the two states increases, which in turn reduces the degree of polarization entanglement. In this section, we study the sole effect of PMD on the concurrence for the optimized waveguide dimensions and therefore find the optimum range for the pump bandwidth corresponding to a particular waveguide length (considering equal rates of generation of $|HH\rangle$ and $|VV\rangle$). It should be emphasized here that the concurrence calculated in the previous sections does not completely evaluate the effect of the pump bandwidth. However, if the output state in Eq. (1) is written in terms of temporal modes and perfect phase matching is assumed at frequencies within the filters, an analytical expression for the concurrence in the presence of a temporal lag in both the signal and the idler arms can be obtained [taking Gaussian functions for the optical filters and pump spectrum; see Eqs. (6) and (7)] and is given by [49,50]

$$C(\tau_s, \tau_i) = \exp \left[\frac{-(\tau_s - \tau_i)^2 \sigma_s^2 \sigma_i^2 - \sigma_p^2 (\tau_s^2 \sigma_s^2 + \tau_i^2 \sigma_i^2)}{8(\sigma_s^2 + \sigma_i^2 + \sigma_p^2)} \right]. \quad (10)$$

The first term is negligible ($\tau_s \cong \tau_i$) due to the low dispersion for both H and V polarizations in the proposed optimum waveguide cross section of $280 \times 770 \text{ nm}^2$.

Figure 6(a) shows the variation of the concurrence as a function of the pump full-width-at-half-maximum (FWHM) bandwidth and the waveguide length for the optimum waveguide cross section of $220 \times 770 \text{ nm}^2$, taking a wavelength detuning (D) of 50 nm around the pump at 1550 nm. The FWHM bandwidths for both of the filters are kept equal and fixed at a typical value of 100 GHz for all the calculations. For a waveguide length of 1 cm (or longer), a pump bandwidth of few gigahertz (1–3 GHz) should be employed to maintain a concurrence > 0.95 in the presence of PMD. In order to employ pump pulses with larger bandwidth, the waveguide length needs to be reduced correspondingly [which can be deduced from Fig. 6(a)] such that $\tau_{s,i} \ll 1/\sigma_p$.

Finally, Fig. 6(b) shows the trade-off between the concurrence and the spectral brightness with the waveguide length for the optimum cross section of $280 \times 770 \text{ nm}^2$ at a detuning of 50 nm from the pump. This shows that the temporal lag accumulated in waveguide lengths $L < 7 \text{ mm}$ can be tolerated, such that a concurrence > 0.95 is achieved, with a pump FWHM bandwidth of 10 GHz. Also, the proposed source is capable of yielding a spectral brightness

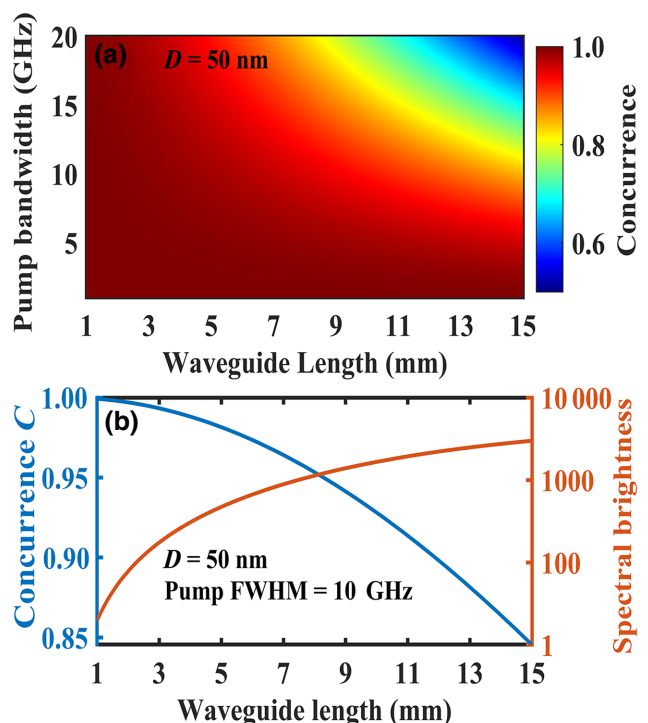


FIG. 6. (a) The concurrence as a function of the pump full-width-at-half-maximum (FWHM) bandwidth and the waveguide length for a cross section of $220 \times 770 \text{ nm}^2$, with a wavelength detuning of 50 nm from the pump at 1550 nm. (b) The concurrence (left axis) and the spectral brightness, i.e., the number of pairs/s/GHz/mW² (right) as a function of the waveguide length for a cross section of $280 \times 770 \text{ nm}^2$ at a detuning of 50 nm, taking a pump FWHM bandwidth of 10 GHz.

of approximately 1000 pairs/s/GHz/mW² in a waveguide of length 10 mm. Note that the spectral brightness is calculated considering equal rates of generation achieved via the optimization techniques proposed in earlier sections of the paper.

IV. CONCLUSIONS

In conclusion, we propose integrated silicon photonic sources for broadband polarization entanglement spanning the S, C, and L bands in the telecommunications spectrum, utilizing SFWM for both H and V polarizations. Silica-clad SOI nanowaveguides with a silicon film thickness of 280–300 nm are shown to support TM₀₀ modes (V polarization) with near-zero GVD (in addition to the fundamental TE₀₀ mode, H polarization) and are thus investigated numerically for concurrence analysis (the degree of entanglement). It is observed that waveguides with a height of 280 nm and a width in the range 700–800 nm are capable of generating a high concurrence > 0.98 for a large wavelength range $> 100 \text{ nm}$ around 1550 nm, whereas the bandwidth yielding a high concurrence (> 0.96) is limited to approximately 40 nm for waveguides with height 300 nm

(with a width in the range 500–550 nm). The polarization angle of the pump is also optimized for further equalization of the generation rates of the orthogonally polarized states $|HH\rangle$ and $|VV\rangle$ and enhancement of the concurrence. Finally, the effect of PMD on the concurrence is studied for the optimized waveguide dimensions. Narrow-band pump pulses with bandwidth $\lesssim 10$ GHz can tolerate the temporal lag accumulated in waveguide lengths $\gtrsim 5$ mm, so that the concurrence remains greater than 0.95 along with a high spectral brightness (approximately 1000 pairs/s/GHz/mW²) for the optimized waveguide devices.

The proposed on-chip sources for generating broadband polarization entanglement in the telecommunications band could be useful for multichannel wavelength-division multiplexed (WDM) entanglement-based quantum key distribution (QKD) protocols utilizing the existing optical-fiber network. This entanglement multiplexing can enhance the data rates and/or the number of simultaneous users in quantum communication. Therefore, these integrated devices are promising building blocks for the implementation of large-scale quantum communication and computation networks.

ACKNOWLEDGMENTS

We gratefully acknowledge the contingent grant of the following funding agencies: the Defence Research and Development Organisation, India [Grant No. DFTM/03/32 03/P/07/JATC-P2QP-07/463/D(R&D)] and the Department of Science and Technology, Ministry of Science and Technology, India [Grant No. DST/ICPS/QuST/Theme-1/2019/Q-62].

-
- [1] C. H. Bennett and S. J. Wiesner, Communication via One- and Two-Particle Operators on Einstein-Podolsky-Rosen States, *Phys. Rev. Lett.* **69**, 2881 (1992).
 - [2] P. G. Kwiat, K. Mattle, H. Weinfurter, A. Zeilinger, A. V. Sergienko, and Y. Shih, New High-Intensity Source of Polarization-Entangled Photon Pairs, *Phys. Rev. Lett.* **75**, 4337 (1995).
 - [3] P. Kok, W. J. Munro, K. Nemoto, T. C. Ralph, J. P. Dowling, and G. J. Milburn, Linear optical quantum computing with photonic qubits, *Rev. Mod. Phys.* **79**, 135 (2007).
 - [4] Y. Yeo and W. K. Chua, Teleportation and Dense Coding with Genuine Multipartite Entanglement, *Phys. Rev. Lett.* **96**, 060502 (2006).
 - [5] D. Bouwmeester, J.-W. Pan, K. Mattle, M. Eibl, H. Weinfurter, and A. Zeilinger, Experimental quantum teleportation, *Nature* **390**, 575 (1997).
 - [6] V. Giovannetti, S. Lloyd, and L. Maccone, Advances in quantum metrology, *Nat. Photonics* **5**, 222 (2011).
 - [7] I. M. Georgescu, S. Ashhab, and F. Nori, Quantum simulation, *Rev. Mod. Phys.* **86**, 153 (2014).
 - [8] J.-W. Pan, D. Bouwmeester, H. Weinfurter, and A. Zeilinger, Experimental Entanglement Swapping: Entangling Photons That Never Interacted, *Phys. Rev. Lett.* **80**, 3891 (1998).
 - [9] A. K. Ekert, Quantum Cryptography Based on Bell's Theorem, *Phys. Rev. Lett.* **67**, 661 (1991).
 - [10] N. Gisin, G. Ribordy, W. Tittel, and H. Zbinden, Quantum cryptography, *Rev. Mod. Phys.* **74**, 145 (2002).
 - [11] E. Knill, R. Laflamme, and G. J. Milburn, A scheme for efficient quantum computation with linear optics, *Nature* **409**, 46 (2001).
 - [12] J. L. O'Brien, A. Furusawa, and J. Vučković, Photonic quantum technologies, *Nat. Photonics* **3**, 687 (2009).
 - [13] L.-T. Feng, G.-C. Guo, and X.-F. Ren, Progress on integrated quantum photonic sources with silicon, *Adv. Quantum Technol.* **3**, 1900058 (2020).
 - [14] N. Matsuda and H. Takesue, Generation and manipulation of entangled photons on silicon chips, *Nanophotonics* **5**, 440 (2016).
 - [15] J. Wang, S. Paesani, Y. Ding, R. Santagati, P. Skrzypczyk, A. Salavrakos, J. Tura, R. Augusiak, L. Mančinska, D. Bacco, D. Bonneau, J. W. Silverstone, Q. Gong, A. Acín, K. Rottwitz, L. K. Oxenløwe, J. L. O'Brien, A. Laing, and M. G. Thompson, Multidimensional quantum entanglement with large-scale integrated optics, *Science* **360**, 285 (2018).
 - [16] J. W. Silverstone, R. Santagati, D. Bonneau, M. J. Strain, M. Sorel, J. L. O'Brien, and M. G. Thompson, Qubit entanglement between ring-resonator photon-pair sources on a silicon chip, *Nat. Commun.* **6**, 1 (2015).
 - [17] H. Takesue, K. Inoue, O. Tadanaga, Y. Nishida, and M. Asobe, Generation of pulsed polarization-entangled photon pairs in a 1.55- μm band with a periodically poled lithium niobate waveguide and an orthogonal polarization delay circuit, *Opt. Lett.* **30**, 293 (2005).
 - [18] A. Yoshizawa, R. Kaji, and H. Tsuchida, Generation of polarisation-entangled photon pairs at 1550 nm using two ppln waveguides, *Electron. Lett.* **39**, 621 (2003).
 - [19] O. Alibart, V. D'Auria, M. De Micheli, F. Doutre, F. Kaiser, L. Labonté, T. Lunghi, É. Picholle, and S. Tanzilli, Quantum photonics at telecom wavelengths based on lithium niobate waveguides, *J. Opt.* **18**, 104001 (2016).
 - [20] K.-i. Harada, H. Takesue, H. Fukuda, T. Tsuchizawa, T. Watanabe, K. Yamada, Y. Tokura, and S.-i. Itabashi, Frequency and polarization characteristics of correlated photon-pair generation using a silicon wire waveguide, *IEEE J. Sel. Top. Quantum Electron.* **16**, 325 (2009).
 - [21] H. Takesue and K. Inoue, 1.5- μm band quantum-correlated photon pair generation in dispersion-shifted fiber: Suppression of noise photons by cooling fiber, *Opt. Express* **13**, 7832 (2005).
 - [22] H. Takesue and K. Inoue, Generation of 1.5- μm band time-bin entanglement using spontaneous fiber four-wave mixing and planar light-wave circuit interferometers, *Phys. Rev. A* **72**, 041804 (2005).
 - [23] Q. Zhou, W. Zhang, J. Cheng, Y. Huang, and J. Peng, Polarization-entangled Bell states generation based on birefringence in high nonlinear microstructure fiber at 1.5 μm , *Opt. Lett.* **34**, 2706 (2009).
 - [24] H. Takesue, Y. Tokura, H. Fukuda, T. Tsuchizawa, T. Watanabe, K. Yamada, and S.-i. Itabashi, Entanglement

- generation using silicon wire waveguide, *Appl. Phys. Lett.* **91**, 201108 (2007).
- [25] S. Sharma, V. Venkataraman, and J. Ghosh, Spectrally-pure integrated telecom-band photon sources in silicon, *IEEE J. Lightwave Technol.* (2022).
- [26] P. Kultavewuti, E. Y. Zhu, X. Xing, L. Qian, V. Pusino, M. Sorel, and J. S. Aitchison, Polarization-entangled photon pair sources based on spontaneous four wave mixing assisted by polarization mode dispersion, *Sci. Rep.* **7**, 1 (2017).
- [27] Q. Zhou, W. Zhang, P. Wang, Y. Huang, and J. Peng, Polarization entanglement generation at $1.5\ \mu\text{m}$ based on walk-off effect due to fiber birefringence, *Opt. Lett.* **37**, 1679 (2012).
- [28] K. Inoue and K. Shimizu, Generation of quantum-correlated photon pairs in optical fiber: Influence of spontaneous raman scattering, *Jpn. J. Appl. Phys.* **43**, 8048 (2004).
- [29] K. F. Lee, J. Chen, C. Liang, X. Li, P. L. Voss, and P. Kumar, Generation of high-purity telecom-band entangled photon pairs in dispersion-shifted fiber, *Opt. Lett.* **31**, 1905 (2006).
- [30] Q. Lin and G. P. Agrawal, Silicon waveguides for creating quantum-correlated photon pairs, *Opt. Lett.* **31**, 3140 (2006).
- [31] H. Fukuda, K. Yamada, T. Shoji, M. Takahashi, T. Tsuchizawa, T. Watanabe, J.-i. Takahashi, and S.-i. Itabashi, Four-wave mixing in silicon wire waveguides, *Opt. Express* **13**, 4629 (2005).
- [32] J. E. Sharping, K. F. Lee, M. A. Foster, A. C. Turner, B. S. Schmidt, M. Lipson, A. L. Gaeta, and P. Kumar, Generation of correlated photons in nanoscale silicon waveguides, *Opt. Express* **14**, 12388 (2006).
- [33] K.-i. Harada, H. Takesue, H. Fukuda, T. Tsuchizawa, T. Watanabe, K. Yamada, Y. Tokura, and S.-i. Itabashi, Generation of high-purity entangled photon pairs using silicon wire waveguide, *Opt. Express* **16**, 20368 (2008).
- [34] H. Takesue, H. Fukuda, T. Tsuchizawa, T. Watanabe, K. Yamada, Y. Tokura, and S.-i. Itabashi, Generation of polarization entangled photon pairs using silicon wire waveguide, *Opt. Express* **16**, 5721 (2008).
- [35] L. Orlslager, J. Safioui, S. Clemmen, K. P. Huy, W. Bogaerts, R. Baets, P. Emplit, and S. Massar, Silicon-on-insulator integrated source of polarization-entangled photons, *Opt. Lett.* **38**, 1960 (2013).
- [36] N. Lv, W. Zhang, Y. Guo, Q. Zhou, Y. Huang, and J. Peng, $1.5\ \mu\text{m}$ polarization entanglement generation based on birefringence in silicon wire waveguides, *Opt. Lett.* **38**, 2873 (2013).
- [37] N. K. Hon, R. Soref, and B. Jalali, The third-order nonlinear optical coefficients of Si, Ge, and $\text{Si}_{1-x}\text{Ge}_x$ in the midwave and longwave infrared, *J. Appl. Phys.* **110**, 9 (2011).
- [38] V. H. Chen, J. R. Ong, and C. E. Png, Polarisation independent silicon-on-insulator slot waveguides, *Sci. Rep.* **6**, 1 (2016).
- [39] See the Supplemental Material at <http://link.aps.org/supplemental/10.1103/PhysRevApplied.18.044043> for more detailed mathematical expressions and some extra results.
- [40] Z. Yang, M. Liscidini, and J. E. Sipe, Spontaneous parametric down-conversion in waveguides: A backward Heisenberg picture approach, *Phys. Rev. A* **77**, 033808 (2008).
- [41] L. G. Helt, M. Liscidini, and J. E. Sipe, How does it scale? comparing quantum and classical nonlinear optical processes in integrated devices, *JOSA B* **29**, 2199 (2012).
- [42] S. Sharma, V. Kumar, P. Rawat, J. Ghosh, and V. Venkataraman, Nanowaveguide designs in 220-nm SOI for ultra-broadband FWM at telecom wavelengths, *IEEE J. Quantum Electron.* **56**, 1 (2020).
- [43] S. R. Petersen, T. T. Alkeskjold, C. B. Olausson, and J. Lægsgaard, Intermodal and cross-polarization four-wave mixing in large-core hybrid photonic crystal fibers, *Opt. Express* **23**, 5954 (2015).
- [44] J. Zhang, Q. Lin, G. Piredda, R. Boyd, G. Agrawal, and P. Fauchet, Anisotropic nonlinear response of silicon in the near-infrared region, *Appl. Phys. Lett.* **91**, 071113 (2007).
- [45] L.-H. Zhang, M. Yang, and Z.-L. Cao, Direct measurement of the concurrence for two-photon polarization entangled pure states by parity-check measurements, *Phys. Lett. A* **377**, 1421 (2013).
- [46] R. Orobtcouk, A. Layadi, H. Gualous, D. Pascal, A. Koster, and S. Laval, High-efficiency light coupling in a submicrometric silicon-on-insulator waveguide, *Appl. Opt.* **39**, 5773 (2000).
- [47] V. R. Almeida, R. R. Panepucci, and M. Lipson, Nanotaper for compact mode conversion, *Opt. Lett.* **28**, 1302 (2003).
- [48] X. Chen and H. K. Tsang, Polarization-independent grating couplers for silicon-on-insulator nanophotonic waveguides, *Opt. Lett.* **36**, 796 (2011).
- [49] M. Shtaif, C. Antonelli, and M. Brodsky, Nonlocal compensation of polarization mode dispersion in the transmission of polarization entangled photons, *Opt. Express* **19**, 1728 (2011).
- [50] M. Brodsky, E. C. George, C. Antonelli, and M. Shtaif, Loss of polarization entanglement in a fiber-optic system with polarization mode dispersion in one optical path, *Opt. Lett.* **36**, 43 (2011).